Full Wave Simulation of Arterial Response under Acoustic Radiation Force

Tuhin Roy and **Murthy N Guddati**[*]
North Carolina State University, Raleigh, NC
[*]Corresponding author, email: mnguddat@ncsu.edu

ABSTRACT

With the ultimate goal of estimating arterial viscoelasticity using shear wave elastography, this paper presents a practical methodology to simulate the response of a human carotid artery under acoustic radiation force (ARF). The artery is idealized as a nearly incompressible viscoelastic hollow cylinder submerged in incompressible, inviscid fluid. For this idealization, we develop a multi-step methodology for efficient computation of three-dimensional response under complex ARF excitation, while capturing the fluid-structure interaction between the arterial wall and the surrounding fluid. The specific steps include (a) performing dimensional reduction through semi-analytical finite element formulation, (b) efficient finite element discretization using traditional and recent techniques. The computational efficiency is further enhanced by utilizing (c) modal superposition, followed by, where appropriate, (d) impulse response function. In addition to developing the methodology, convergence analysis is performed for a typical arterial geometry, leading to recommendations on various discretization parameters. At the end, the computational effort is shown to be several orders of magnitude less than the traditional, fully three-dimensional analysis using finite element methods, leading to a practical yet accurate simulation of arterial response under ARF excitations.

Keywords: Arterial stiffness; Guided waves; Semi-analytical finite element method; Shear wave elastography; Viscoelasticity

INTRODUCTION

Arterial stiffness is one of the important biomarkers for many cardiovascular diseases [1–5]. Among various non-invasive approaches, Shear Wave Elastography (SWE, [6]) is one of the effective techniques to characterize arterial stiffness. Specifically, the arterial wall motion data is processed to obtain the dispersion curve (phase velocity variation as a function of frequency), which is then used to invert for arterial wall modulus. While this approach works well for estimating the elasticity part of the arterial wall modulus, it fails to quantify viscosity, as the phase velocities are not much sensitive to arterial viscosity [7]. One way to quantify full viscoelasticity is by matching the measured and simulated arterial wall motions (this is because spatial distribution and history of wall motion are sensitive not only to elasticity but also to viscosity, see e.g. [8]). Towards the end goal of viscoelastic inversion, the focus of the paper is the computation of tube wall motion distribution and history under acoustic radiation force (ARF) excitation. While such simulation can certainly be performed using 3D finite elements, it would be computationally very expensive, making practical inversion prohibitive. Thus, to facilitate practical viscoelastic inversion from the space-time data, we develop a methodology that is orders of magnitude more efficient than 3D finite element simulation.

Several analytical formulations [9–15] are available for elastic and acoustoelastic waveguides (elastic waveguides immersed in acoustic fluid) but they are limited to simple geometries. Computational simulation is often necessary when the geometry, boundary conditions or material properties are more complicated. Among the several variants of the finite element methods, we consider the Semi-Analytical Finite Element method (SAFE, see e.g. [16–22]). The idea of SAFE method is to utilize analytical formulation in a few direction(s) while the finite element discretization in the remaining direction(s). SAFE method can be utilized effectively to model wave propagation in a carotid artery, where the material properties along the axial and azimuthal directions can be assumed to be homogeneous. Essentially, we employ Fourier expansion in axial and azimuthal directions, and finite element discretization is used only in the radial direction. This makes the SAFE model extremely efficient compared to the traditional 3D finite element models.

For the finite element discretization in the radial discretization, we adapt (1) high-order finite elements for the arterial wall and the inner fluid, given the smoothness of the response, (2) Perfectly Matched Discrete Layers (PMDL) for efficiently simulating the large region containing the exterior fluid. The resulting discrete dynamical system is solved using modal superposition where a few eigenmodes are shown to be sufficient to capture the dynamics of the system, leading to a further reduction in the computational cost. For the simpler Voigt model, we can solve the resulting single-degree-of-freedom (SDOF) problem using convolution with impulse response function (Green's function in the time domain), resulting in an extremely efficient simulation methodology. For more complicated fractional viscoelastic models, we solve the problem using frequency domain computation followed by inverse Fourier transform, which tends to be more expensive but still practical.

The outline of the remainder of the paper is as follows. We first present the governing differential equations, interface and boundary conditions that represent the physics of the problem. Next, the proposed methodology is described in detail. In the following section, numerical experiments are utilized to examine the convergence of the methodology, leading to recommended discretization parameters for the carotid artery problem. In the final section, we summarize the proposed methodology and future work.

PROBLEM STATEMENT

The carotid artery is made of biological tissue where the pressure wave velocity is two orders of magnitude larger than the shear wave velocity. The contrast is higher for the surrounding tissue and blood, where the shear wave velocity and viscosity are much smaller than that of the arterial wall. Given these observations, the artery can be approximated as a nearly incompressible viscoelastic cylindrical waveguide filled with and immersed in incompressible inviscid fluids. The schematic of the model is shown in Figure 1. The governing differential equation for the solid medium is the Elastodynamic equation, written here in the frequency domain as,

$$\mathbf{L}_{\sigma}^{T}\boldsymbol{\sigma} - \rho\omega^{2}\mathbf{u} = \mathbf{f}, \text{ in } \Omega_S \text{ ,} \tag{1}$$

where the primary variable in the solid domain (Ω_S) is the displacement vector, $\boldsymbol{u} = \boldsymbol{u}(r,\theta,z,\omega)$ with three components, i.e., $\boldsymbol{u} = \{u_r, u_\theta, u_z\}^T$. ρ is the density of the solid medium. $\mathbf{f} = \mathbf{f}(r,\theta,z,\omega)$ is the spatially and temporally varying acoustic radiation force, which can be computed e.g., using software such as Field II [23,24]. $\boldsymbol{\sigma} = \lambda \mathrm{tr}(\boldsymbol{\varepsilon}) I + 2G\boldsymbol{\varepsilon}$ is the stress tensor, where, $\boldsymbol{\varepsilon}$ is the strain tensor (written in vector form), and $\boldsymbol{\varepsilon} = \mathbf{L}_{\varepsilon}\boldsymbol{u} = \{\varepsilon_{rr}, \varepsilon_{\theta\theta}, \varepsilon_{zz}, \varepsilon_{\theta z}, \varepsilon_{rz}, \varepsilon_{r\theta}\}^T$. For the materials considered here, $\lambda >> G$, and can be assumed to be constant and given by $\lambda \approx \rho c_p^2$, where c_p is the acoustic (pressure) wave velocity and taken as 1540 m/s. In the time domain, the shear modulus is in general integro-differential operator but takes the simple form of frequency-dependent complex modulus when transformed into the frequency domain. For the Voigt model, the modulus can be written as,

$$G(\omega) = G_0(1 + i\omega\tau) \ , \tag{2}$$

where G_0 is the elastic modulus and τ is the relaxation time (representing viscosity). For fractional model such as the spring-pot model, the frequency-dependent shear modulus can be written as,

$$G(\omega) = G_0\left(\frac{i\omega}{\omega_0}\right)^{\alpha} = G_0\left(\frac{\omega}{\omega_0}\right)^{\alpha}\left(\cos\left(\alpha\frac{\pi}{2}\right) + i\sin\left(\alpha\frac{\pi}{2}\right)\right) , \tag{3}$$

where α is the fractional order, ω_0 is the normalization frequency, and G_0 is the modulus (note that the G_0 in Equation (2) and (3) are different). While the approach proposed in this paper works for any viscoelastic model, we choose the above two models as representative examples since they are the building blocks for the higher order models that are frequently used for modeling soft tissues [25]. The $\mathbf{L}_{\sigma}$ and $\mathbf{L}_{\varepsilon}$ are 6×3 gradient operators given by,

$$\begin{aligned}
\mathbf{L}_{\varepsilon} &= \mathbf{L}_r \frac{\partial(.)}{\partial r} + \mathbf{L}_{\theta}\frac{1}{r}\frac{\partial(.)}{\partial\theta} + \mathbf{L}_z\frac{\partial(.)}{\partial z} + \mathbf{L}_0\frac{1}{r},\\
\mathbf{L}_{\sigma} &= \mathbf{L}_r \frac{1}{r}\frac{\partial(.\times r)}{\partial r} + \mathbf{L}_{\theta}\frac{1}{r}\frac{\partial(.)}{\partial\theta} + \mathbf{L}_z\frac{\partial(.)}{\partial z} - \mathbf{L}_0\frac{1}{r},\\
&L_r(1,1) = L_r(5,3) = L_r(6,2) = 1,\\
&L_{\theta}(2,2) = L_{\theta}(4,3) = L_{\theta}(6,1) = 1,\\
&L_z(3,3) = L_z(4,2) = L_z(5,1) = 1,\\
&L_o(2,1) = -L_o(6,2) = 1.
\end{aligned} \tag{4}$$

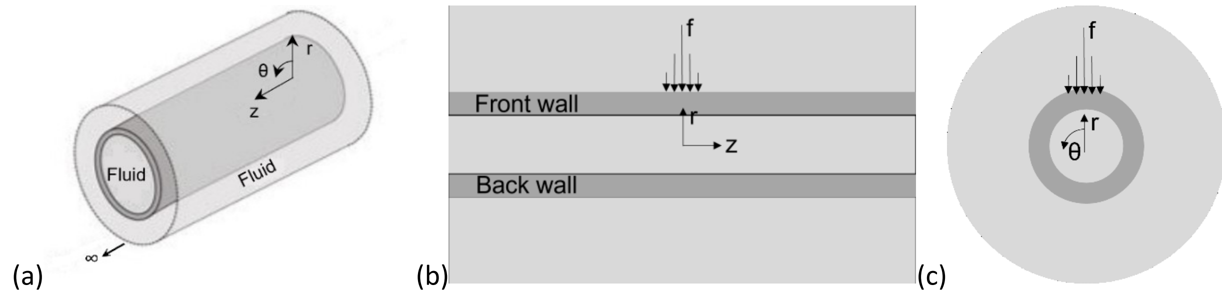

Figure 1. (a): schematic of the idealized artery. (b): longitudinal view with the acoustic radiation force (ARF). (c): cross-sectional view with ARF.

For the fluid domain, in the limit of incompressibility, the acoustic wave equation becomes the Laplace equation,

$$\nabla^2 p = 0 \text{ in } \Omega_F \ , \tag{5}$$

where the primary variable in the fluid domain (Ω_F) is the pressure, $p = p(r,\theta,z,\omega)$. The Laplace operator in cylindrical coordinate systems is, $\nabla^2(\cdot) = r^{-1}\partial(r\partial(\cdot)/\partial r)/\partial r + r^{-2}\partial^2(\cdot)/\partial\theta^2 + \partial^2(\cdot)/\partial z^2$. The conditions at the solid-fluid interfaces Γ_{SF} are the traction continuity:

$$\boldsymbol{\sigma}\cdot\mathbf{n}_s - p\mathbf{n}_F = 0, \text{ on } \Gamma_{SF} \ , \tag{6}$$

and the continuity of the normal displacement, equivalently acceleration:

$$-\omega^2\mathbf{u}\cdot\mathbf{n}_s - \frac{1}{\rho_F}\frac{\partial p}{\partial\mathbf{n}_F} = 0, \text{ on } \Gamma_{SF} \, . \tag{7}$$

$\mathbf{n}_s$ and $\mathbf{n}_F = -\mathbf{n}_S$ are the unit vectors for solid and fluid domains respectively. ρ_F is the fluid density.

Given the tube geometry, applied loading, and material properties of the tube, inside and outside fluids, our objective is to compute the wall velocity in the spatiotemporal domain. The proposed approach is detailed in the following section.

METHODOLOGY

We solve the Equations (1) and (5) to (7) along with radiation condition in four steps: (1) model reduction and discretization using the Semi-Analytical Finite Element (SAFE) method and Perfectly Matched Discrete Layers (PMDL), (2) further decoupling into single-degree-of-freedom systems through modal analysis, (3) finding the temporal response for each mode, and (4) computing the final response in space-time by superimposing all the modal responses. The details of each step are presented in the following subsections.

Spatial Discretization through SAFE and PMDL

Owing to the invariant geometry and material properties along the axial and azimuthal direction of the tube, we utilize Fourier expansion in these two directions and employ finite element discretization in the radial direction. This falls in the realm of the Semi-Analytical Finite Element (SAFE) method [16,26,27]. For the surrounding unbounded fluid, we consider Perfectly Matched Discrete Layers (PMDL, [28,29]).

Facilitated by the Fourier expansions in the axial and azimuthal directions, the discretized displacement is written as,

$$\mathbf{u}(r,\theta,z,t)=\int_{\omega=-\infty}^{\omega=+\infty}\int_{k=-\infty}^{k=+\infty}\sum_{m=0}^{m=\infty}\mathbf{N}_S(r)\begin{bmatrix}\mathbf{U}_r(m,k,\omega)\cos(m\theta)\\ \mathbf{U}_\theta(m,k,\omega)\sin(m\theta)\\ \mathbf{U}_z(m,k,\omega)\cos(m\theta)\end{bmatrix}e^{-ikz}e^{i\omega t}dk\,d\omega\ , \tag{8}$$

where m is the circumferential Fourier number, k is the wavenumber along the axial direction (z). Note that the sine variation of u_θ and cosine variation in other components are driven by the fact that the load and thus the response is symmetric about $\theta=0$. In the fluid medium, the discretized pressure variable becomes,

$$p(r,\theta,z,t)=\int_{\omega=-\infty}^{\omega=+\infty}\int_{k=-\infty}^{k=+\infty}\sum_{m=0}^{m=\infty}\mathbf{N}_F(r)\mathbf{P}(m,k,\omega)\,cos(m\theta)e^{-ikz}e^{i\omega t}dk\,d\omega, \tag{9}$$

where $\mathbf{N}_S$ and $\mathbf{N}_F$ are the finite element shape function matrices in the solid and fluid domain, respectively. For the fluid domain, we employ regular finite elements for the inner region and PMDL for the outer region (which naturally incorporates the radiation condition, see [28,29]). The response is expected to vary smoothly inside the wall, leading us to choose higher order finite elements (their effectiveness is illustrated in convergence analysis presented in a subsequent section). For the solid medium, the discretized form of Equation (1) becomes,

$$\left(k^2\mathbf{K}^{S2}+ik\ \mathbf{K}^{S1}+\mathbf{K}^{S0}\right)\mathbf{U}_m+\left(-\kappa\mathbf{C}_{SF}\right)\mathbf{P}_m-\omega_m^2\mathbf{M}^S\mathbf{U}_m=\mathbf{F}_m\ , \tag{10}$$

where,

$$\begin{gathered}\mathbf{K}^{S1}=\int_\Omega\left(\mathbf{B}_r+\mathbf{B}_\theta\right)^T\mathbf{D}\mathbf{B}_z r\,dr\,d\theta-\int_\Omega\mathbf{B}_z^T\mathbf{D}\left(\mathbf{B}_r+\mathbf{B}_\theta\right)r\,dr\,d\theta,\\ \mathbf{K}^{S0}=\int_\Omega\left(\mathbf{B}_r+\mathbf{B}_\theta\right)^T\mathbf{D}\left(\mathbf{B}_r+\mathbf{B}_\theta\right)r\,dr\,d\theta,\quad \mathbf{K}^{S2}=\int_\Omega\mathbf{B}_z^T\mathbf{D}\mathbf{B}_z r\,dr\,d\theta,\end{gathered} \tag{11}$$

In the above, $\mathbf{D}$ is the constitutive matrix, i.e., $\boldsymbol{\sigma}=\mathbf{D}\boldsymbol{\epsilon}$. $\mathbf{B}_r,\mathbf{B}_\theta,\mathbf{B}_z$ are given by,

$$\mathbf{B}_r=\mathbf{L}_r\frac{\partial\mathbf{N}_S}{\partial r},\ \mathbf{B}_\theta=\mathbf{L}_\theta\frac{\mathbf{N}_S}{r}+\mathbf{L}_0\frac{\mathbf{N}_S}{r},\ \mathbf{B}_z=-\mathbf{L}_z\mathbf{N}_S\ , \tag{12}$$

where,

$$\tilde{\mathbf{L}}_{\theta} = \mathbf{L}_{\theta} m \begin{bmatrix} -\sin(m\theta) & 0 & 0 \\ 0 & \cos(m\theta) & 0 \\ 0 & 0 & -\sin(m\theta) \end{bmatrix}. \quad (13)$$

κ in Equation (10) is the scaling factor introduced to better condition the matrix by maintaining the similar numerical orders of the solid and fluid domain contributions. The solid-fluid interaction matrix is,

$$\mathbf{C}_{SF} = \int_{\Omega} \mathbf{N}_S^T \mathbf{n}_f \mathbf{N}_F r dr d\theta \ . \quad (14)$$

The discretized force vector on the right side of Equation (10) is,

$$\mathbf{F}_m = \int_{\Omega} \mathbf{N}_S{}^T f_m r dr d\theta , \quad (15)$$

where f_m is the forcing function corresponding to the m^{th} circumferential mode. The discretized form of Equation (5) after incorporating the interface condition is,

$$\kappa\left(k^2 \mathbf{K}^{F2} - \mathbf{K}^{F0}\right)\mathbf{P}_m - \omega_m^2 \mathbf{C}_{SF}^T \mathbf{U}_m = \mathbf{0} , \quad (16)$$

where,

$$\mathbf{K}^{F2} = \int_r \mathbf{N}_F^T \mathbf{N}_F r dr d\theta, \quad \mathbf{K}^{F0} = m^2 \int_r \frac{1}{r^2} \mathbf{N}_F^T \mathbf{N}_F r dr d\theta + \int_r \left(\frac{\partial \mathbf{N}_F}{\partial r}\right)^T \left(\frac{\partial \mathbf{N}_F}{\partial r}\right) r dr d\theta \ . \quad (17)$$

Note that the scaling factor κ is used here again to better condition the final coefficient matrix. After assembling, the final discretized system takes the form,

$$\left(\mathbf{K} - \omega_m^2 \mathbf{M}\right) \begin{Bmatrix} \mathbf{U}_m \\ \mathbf{P}_m \end{Bmatrix} = \begin{Bmatrix} \mathbf{F}_m \\ \mathbf{0} \end{Bmatrix}, \quad (18)$$

where,

$$\mathbf{K} = \begin{bmatrix} k^2 \mathbf{K}^{S2} + ik\,\mathbf{K}^{S1} + \mathbf{K}^{S0} & -\kappa \mathbf{C}_{SF} \\ \mathbf{0} & \kappa\left(k^2 \mathbf{K}^{F2} - \mathbf{K}^{F0}\right) \end{bmatrix}, \quad \mathbf{M} = \begin{bmatrix} \mathbf{M}^S & \mathbf{0} \\ \mathbf{C}_{SF}^T & \mathbf{0} \end{bmatrix}. \quad (19)$$

Modal Decomposition

Given the expected smoothness of the response within the thickness of the wall, we hypothesize modal superposition approach would lead to computation with only a few modes, leading to computational savings (this is confirmed using convergence analysis in a later section). The modes are computed from the associated eigenvalue problem:

$$\left(\mathbf{K} - \omega^2 \mathbf{M}\right) \mathbf{\Phi}(k, m) = \mathbf{0} , \quad (20)$$

where $\mathbf{\Phi}$ is the matrix containing mode shapes. The resulting discretized deformation $\mathbf{U}$ can be computed through superimposing all the modal responses:

$$\begin{Bmatrix} \mathbf{U}_m \\ \mathbf{P}_m \end{Bmatrix} = \sum_{i=1}^{N} \gamma_i(\omega) \boldsymbol{\phi}_i(k,m) , \tag{21}$$

where N is the total number of modes. Substituting Equation (21) into the Equation (20) and utilizing orthogonality property of the modes, we obtain the governing equation for the i^{th} modal participation factor γ_i:

$$k_i\gamma_i - \omega^2 m_i\gamma_i = f_i \ , \tag{22}$$

where, $k_i = \boldsymbol{\phi}_i^T \mathbf{K} \boldsymbol{\phi}_i$, $m_i = \boldsymbol{\phi}_i^T \mathbf{M} \boldsymbol{\phi}_i$, and $f_i = \boldsymbol{\phi}_i^T \mathbf{F}$ are the modal stiffness, mass, and force respectively.

Temporal Response

To get the temporal response, we apply inverse Fourier transformation on the vector computed from Equation (21) to transform back to the time domain:

$$\bar{\mathbf{U}}(k,m,t) = \int_{-\infty}^{\infty} \mathbf{U}(k,m,\omega) e^{2\pi i \omega t} d\omega \ . \tag{23}$$

Numerically, we achieve this through utilizing the Fast Fourier transform. While this approach works for any viscoelastic model, for the Voigt model, we can utilize the more efficient Green's function (Impulse Response Function, IRF) approach directly in the time domain. To this end, we consider the time domain representation of Equation (22), for the Voigt model, where the (frequency dependent) stiffness term k_i transforms to $\bar{k}_i + c_i \, d/dt$, resulting in,

$$\bar{k}_i\gamma_i + c_i \frac{\partial \gamma_i}{\partial t} + m_i \frac{\partial^2 \gamma_i}{\partial t^2} = f_i \ , \tag{24}$$

where, the modal stiffness is, $\bar{k}_i$ corresponds to $\int B^T G_0 B r dr d\theta$ part of the stiffness matrix, while modal damping c_i corresponds to $\int B^T G_0 \tau B r dr d\theta$ part of the stiffness matrix. The impulse response function is then given by,

$$IRF_{u,i}(t) = \frac{1}{m\omega_i} \sin(\omega_i t) e^{-\beta_i t} \ , \tag{25}$$

where ω_i and β_i are the (damped) natural frequency and decay rate respectively, and are given by,

$$\omega_i = \frac{\sqrt{4 m_i \bar{k}_i - c_i^2}}{2 m_i}, \quad \beta_i = \frac{c_i}{2 m_i} \ . \tag{26}$$

The final time domain mode participation factor is the convolution of the impulse response function with the forcing function:

$$\gamma_i(t) = \int_0^t f_i(\bar{t}) IRF_{u,i}(t-\bar{t}) d\bar{t} \ . \tag{27}$$

$\dot{\gamma}_i(t)$, the time derivative of the modal participation factor would be useful for computing velocity response, and can be computed similarly by replacing the IRF with its time derivative:

$$\begin{aligned} IRF_{v,i}(t) &= \frac{1}{m\omega_i}\left(\cos(\omega_i t) - \beta_i \sin(\omega_i t)\right) e^{-\beta_i t}, \\ \dot{\gamma}_i(t) &= \int_0^t f_i(\bar{t}) IRF_{v,i}(t-\bar{t}) d\bar{t}. \end{aligned} \tag{28}$$

Final Response in Space-time

The wavenumber-time (k-t) representation of the wall response is first obtained by superposition of the temporal response of all the modes:

$$\mathbf{U}(k,t) = \sum_{m=0}^{M}\sum_{i=1}^{N} \gamma_{i,m}(t)\,(\boldsymbol{\phi}_{i,m})\left[\cos(m\theta), \sin(m\theta), \cos(m\theta)\right]^T \ . \tag{29}$$

Applying inverse Fourier transform in space results in the final displacement $\mathbf{U}(z,t)$. The velocity response can similarly be obtained by replacing $\gamma_{i,m}(t)$ by $\dot{\gamma}_{i,m}(t)$.

CONVERGENCE STUDY AND RECOMMENDED DISCRETIZATION

In addition to developing the general methodology presented in the previous section, we attempt to provide general recommendation for various discretization parameters. To this end, given that the arterial geometry does not have large variation, we consider a typical geometry of rubber tubes considered in recent studies [6,30], with the expectation that the recommended parameters would be applicable for various human carotid arteries, undergoing SWE investigation with typical ARF excitation and data acquisition.

To mimic typical ARF excitation that is sharp in the axial direction and somewhat spread out in the azimuthal direction ([31]), we consider the excitation force to vary in (z,θ) as Gaussian, which is plotted in Figure 2. Examining the Fourier coefficients in (b) and (d), we note that the forcing is limited to a narrow band in the Fourier domain, indicating that our framework based on Fourier basis functions would be efficient. The temporal variation of the forcing function is assumed to be rectangular with a pulse width of 400 microseconds, as shown in Figure 3, which is fairly consistent with the way acoustic radiation is applied (sudden illumination followed by sudden shutoff). Given that the focus area is typically much larger than the entire wall thickness, the variation of the force within the wall in the radial direction is assumed to be uniform.

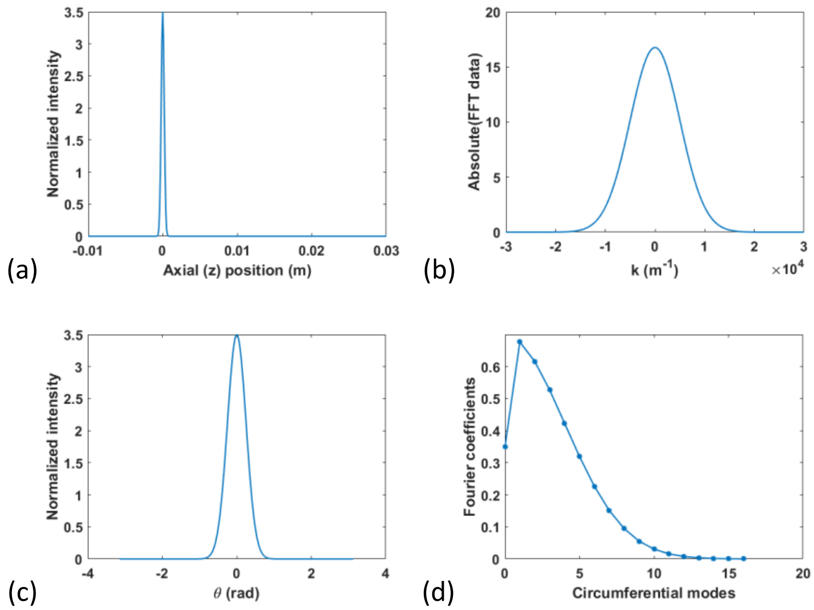

Figure 2. Applied excitation force (normal pressure on the wall): (a) variation in the axial direction (z); (b) corresponding Fourier transform; (c) variation in the circumferential θ direction; (d) corresponding Fourier coefficients.

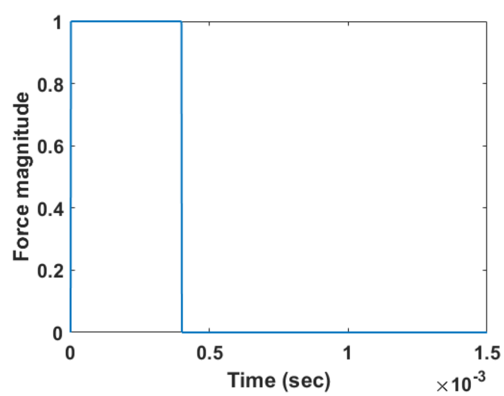

Figure 3. Acoustic radiation force variation in time.

To obtain discretization parameters that can be routinely used for simulating human carotid arteries, we consider a typical geometry of a cylindrical tube with a wall thickness of 1 mm, and an inner radius of 3 mm. The density is assumed to be 1,000 kg/m^3 for both solid and fluid media. The two viscoelastic models are considered for the wall material: (a) Voigt model with an elastic modulus (G_0) of 200 kPa and a relaxation time (τ) of 0.055 ms and (b) spring-pot model with a fractional order (α) of 0.15, and a modulus (G_0) of 344 kPa at 600 Hz (the parameter values are in the range of the artery mimicking phantom material [30]). The frequency-dependent shear moduli are presented in Figure 4.

The convergence analysis is performed by first obtaining the reference solution ($v_{reference}$) with the highest-refined parameters (defined below) and then performing analysis by successive refinement with respect to the discretization parameter of interest. The highest-refined parameters are: maximum number of circumferential modes (m_{max}) = 14; maximum wavenumber (k_{max}) = 30,000 m^{-1} ; minimum wavenumber increment (Δk_{min}) = 10 m^{-1} ; maximum finite element order (p_{max}) for solid-domain = 14; p_{max} for inside fluid = 5; maximum PMDL elements for outside fluid = 11. For the eigenmode expansion, we take all the modes i.e., there is no modal truncation in computing the reference solution. The error is defined in terms of the maximum velocity $\left(v^{\max}\right)$, which is more stringent than, e.g., least-squares error (specific expressions for error measures are provided later). We perform the convergence analysis for each of the parameters, with the objective of obtaining the response with a practically acceptable error of 1% (consistent with the expected variability and noise levels). As detailed below, the convergence analysis is performed for circumferential and longitudinal wavenumbers, finite element discretization for solid, the inner and outer fluid domains separately, followed by convergence analysis of radial eigenmode expansion.

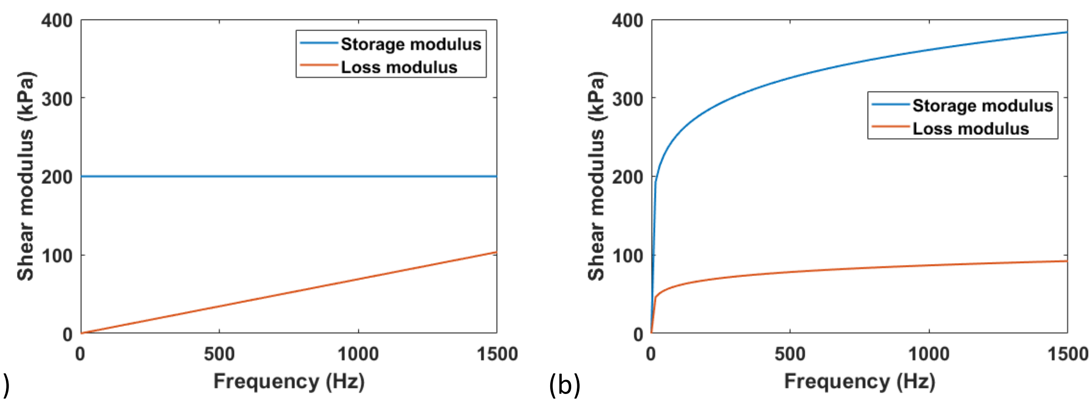

Figure 4. Input shear moduli corresponding to the Voigt model (a) and the spring-pot model (b).

Circumferential mode convergence. The normalized error from the circumferential mode convergence study is presented in Figure 5 (a). Here the normalized error is computed as,

$$E_m = \frac{\| v_{reference}^{max} - v_m^{max} \|_2}{\| v_{reference}^{max} \|_2} \ , \tag{30}$$

where we consider the lowest m circumferential modes to compute the maximum velocity v_m^{max}. As shown in Figure 5 (a), with the lowest 8 circumferential modes, we achieve a normalized error of 1%.

Longitudinal wavenumber convergence. We now study the convergence with respect to the longitudinal wavenumber, k. The analysis is performed in two steps: (1) convergence with the maximum wavenumber, k_{max}, and (2) the wavenumber increment, Δk. The results are shown in Figure 5 (b) and (c). The normalized error shown in the figure is computed as,

$$E_{k_{max}} = \frac{\| v_{reference}^{max} - v_{k_{max}}^{max} \|_2}{\| v_{reference}^{max} \|_2} \ , \tag{31}$$

$$E_{\Delta k} = \frac{\| v_{reference}^{max} - v_{\Delta k}^{max} \|_2}{\| v_{reference}^{max} \|_2} \, , \tag{32}$$

where, $E_{k_{max}}$ and $E_{\Delta k}$ are the normalized error associated with k_{max} and Δk respectively. After examining Figure 5 (b) and (c), for an error of 1%, $k_{max} = 10,000 \ m^{-1}$ and $\Delta k = 40 \ m^{-1}$ appear to be conservative choices.

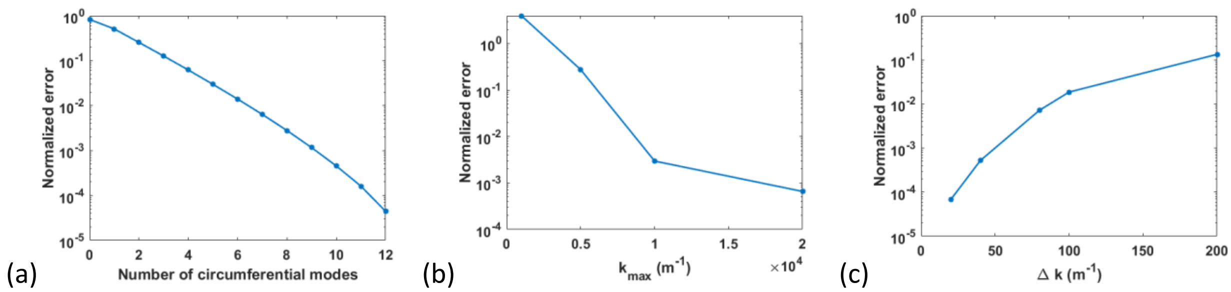

Figure 5. Convergence results of circumferential Fourier number (a), maximum longitudinal wavenumber (b), and the step size associated with longitudinal wavenumber (c).

Solid domain mesh convergence. The convergence of the response due to increasing the polynomial order of the shape function in the solid medium is considered. The normalized error is in the context is taken as,

$$E_p = \frac{\| v_{reference}^{max} - v_p^{max} \|_2}{\| v_{reference}^{max} |_2} \, , \tag{33}$$

where p is the polynomial order. The convergence result is presented in Figure 6 (a), which indicates that 9 noded finite element (*p=8*) is sufficient for an engineering accuracy of 1%.

Inner fluid mesh convergence. The mesh convergence study is also performed for the interior fluid domain by examining the relative error,

$$E_p = \frac{\| v_{reference}^{max} - v_p^{max} \|_2}{\| v_{reference}^{max} \|_2} \, , \tag{34}$$

where p is the polynomial order for the finite element shape function in the interior fluid domain. The convergence result is presented in Figure 6 (b), indicating that 3 noded (quadratic) finite elements are sufficient for the interior fluid domain, to achieve an accuracy of 1%.

Outer fluid (PMDL) mesh convergence. In this section, the mesh convergence is performed only for the outside fluid domain (PMDL). Although the geometric progression ratio affects PMDL accuracy, we kept a smaller progression ratio of 1.5, which is shown to result in a negligible error of less than 10^{-7} [32]. The convergence study is performed only for the number of PMDL elements. The normalized error is defined as,

$$E_d = \frac{\| v_{reference}^{max} - v_d^{max} \|_2}{\| v_{reference}^{max} \|_2} \quad , \tag{35}$$

where d is the number of PMDL elements. The convergence result is presented in Figure 6 (c), indicating that 7 PMDL elements are sufficient to achieve the engineering accuracy of 1%.

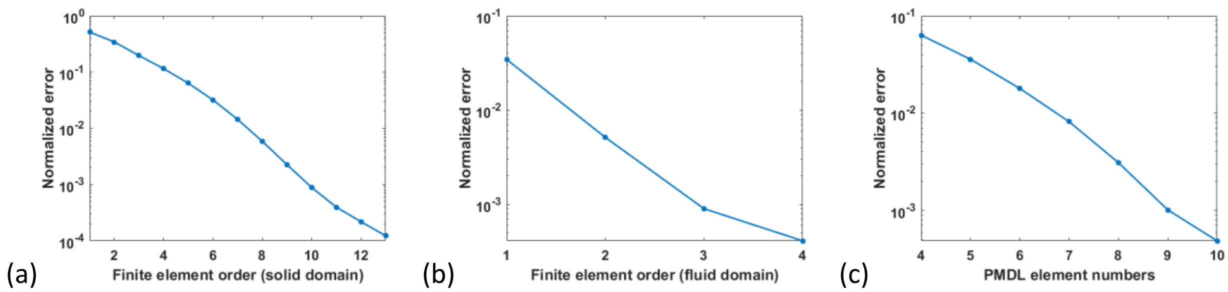

Figure 6. Convergence results of polynomial order of the finite element shape function for the solid domain (a), and the inside fluid domain (b). PMDL mesh convergence results for the outside fluid domain (c).

Radial eigenmode convergence. In this section, we study the convergence of the number of eigenmodes. The normalized error is computed as,

$$E_n = \frac{\| v_{reference}^{max} - v_n^{max} \|_2}{\| v_{reference}^{max} \|_2} \quad , \tag{36}$$

where *n* is the number of eigenmodes considered. The convergence result is presented in Figure 7. As observed, the first 17 modes are sufficient to achieve an engineering accuracy of 1%.

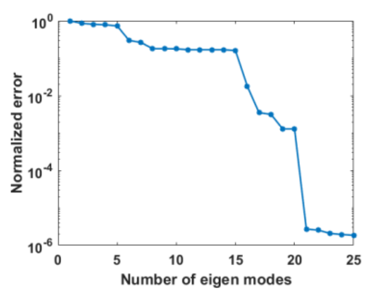

Figure 7 Convergence results of radial eigenmode expansion

Recommended Discretization. To summarize, based on the above convergence analyses, to compute the wall motion with an engineering accuracy of 1%, it appears sufficient to use 0th to 7th circumferential modes, longitudinal wavenumbers up to $k_{max} = 10,000\ m^{-1}$ with $\Delta k = 40\ m^{-1}$, single 8th order (9-noded) finite element for the arterial wall, single quadratic (3-noded) finite element in the fluid domain, and 7 PMDL elements for the exterior fluid. To further reduce the computational cost, one can limit the computation to the first 17 eigenmodes.

Computational Cost. With seven 3.4 GHz cores on a standard desktop computer, a single simulation takes less than 5 seconds for the Voigt model (for the spring-pot model, it takes less than 84 seconds). The 3D finite element approach for the Voigt model takes about 361 seconds with 48 3.1 GHz processors, as mentioned in [33]. Assuming 80% parallel efficiency, the proposed approach with the Voigt model is approximately 400 times faster than the 3D finite element approach. Moreover, note that the 3D finite element model is likely more approximate than the proposed model due to, e.g., higher discretization errors and spurious reflections from primitive absorbing boundary conditions. It is likely that the efficiency gain would be even more for comparable accuracy.

Representative Results. With the recommended parameters, the full wave velocity response corresponding to the front wall is presented in Figure 8. These results are qualitatively similar to the responses observed in SWE experiments (see e.g. [34]).

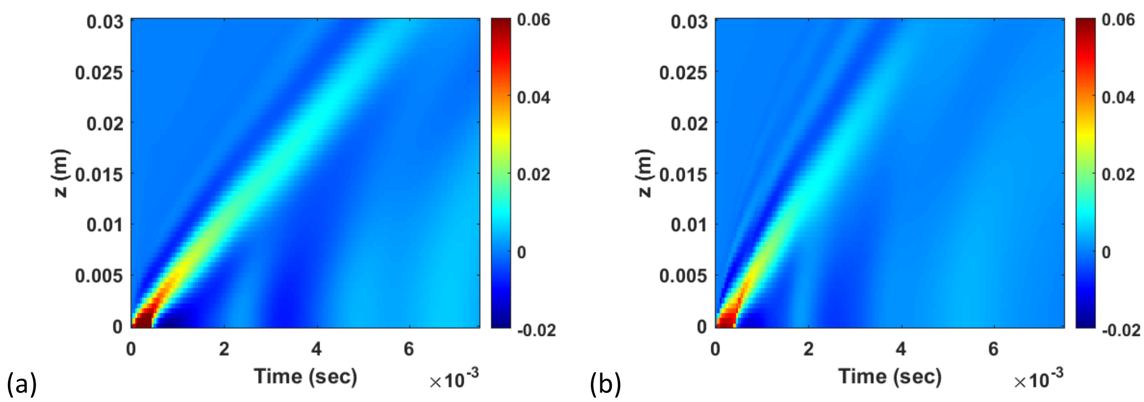

Figure 8. x-t representation of the top wall velocity from the proposed approach.
(a): Voigt model. (b): spring-pot model.

CONCLUSIONS

With the ultimate goal of estimating arterial viscoelasticity by matching measured and simulated motion data, we present a computationally efficient framework to simulate arterial wall motion under acoustic radiation push. After idealizing the artery as an incompressible viscoelastic cylinder immersed in inviscid fluid, we combine multiple computational techniques to perform fully three-dimensional simulation in a very short time (5 seconds when a Voigt model is used, and 84 seconds for a more complicated spring-pot model). The steps involved are: (a) Fourier series expansion in the azimuthal direction, (b) Fourier transform in the axial direction, (c) high-order finite element discretization for the wall and interior fluid and special finite elements (PMDL) for exterior fluid, (d) modal truncation to further reduce the computational cost, and (e) impulse-response or frequency-response approach to solve the final set of single-degree of freedom vibration problems. At the end, the full three-dimensional response is captured, at a tiny fraction of the computational cost of e.g., the three-dimensional finite element method. With such computational cost savings, inversion of shear-wave elastography data can be performed with reasonable computational effort, eventually making the process practical on clinical scanners (inversion using the proposed computational model is performed in [8]).

While the proposed model simulates artery mimicking phantoms (see [34]), several future improvements can be considered. Some of the potential areas of expansion include: (a) viscoelasticity of the surrounding tissue, (b) viscosity of blood, (c) anisotropy of the arterial wall, (d) heterogeneity of the arterial wall, e.g., differentiation of intima, media, and adventitia, and (e) modeling plaque formation or thrombosis. Item (e) may require expansion to 2D finite element modeling of cross-section (see e.g. [35]) or necessitate a full 3D model. On the other hand, aspects (a) to (d) could be tackled with the proposed approach and can be subjects of future research.

ACKNOWLEDGEMENTS

The work is partially funded by the National Science Foundation grant DMS-2111234, and by the National Institute of Health grant 5R01 HL145268. The content is solely the responsibility of the authors and does not necessarily represent the official views of the National Science Foundation or the National Heart, Lung, and Blood Institute or the National Institutes of Health.

REFERENCES

[1] S. Laurent, P. Boutouyrie, R. Asmar, I. Gautier, B. Laloux, L. Guize, P. Ducimetiere, A. Benetos, Aortic stiffness is an independent predictor of all-cause mortality in hypertensive patients, J. Hypertens. 18 (2000).

[2] K.S. Cheng, C.R. Baker, G. Hamilton, A.P.G. Hoeks, A.M. Seifalian, Arterial elastic properties and cardiovascular risk/event, Eur. J. Vasc. Endovasc. Surg. 24 (2002) 383–397. https://doi.org/10.1053/ejvs.2002.1756.

[3] B.A. Kingwell, C.D. Gatzka, Arterial stiffness and prediction of cardiovascular risk, J. Hypertens. 20 (2002).

[4] K. Sutton-Tyrrell, S.S. Najjar, R.M. Boudreau, L. Venkitachalam, V. Kupelian, E.M. Simonsick, R. Havlik, E.G. Lakatta, H. Spurgeon, S. Kritchevsky, M. Pahor, D. Bauer, A. Newman, Health ABC Study, Elevated aortic pulse wave velocity, a marker of arterial stiffness, predicts cardiovascular events in well-functioning older adults., Circulation. 111 (2005) 3384–90. https://doi.org/10.1161/CIRCULATIONAHA.104.483628.

[5] E. Dolan, L. Thijs, Y. Li, N. Atkins, P. McCormack, S. McClory, E. O'Brien, J.A. Staessen, A. V Stanton, Ambulatory arterial stiffness index as a predictor of cardiovascular mortality in the Dublin Outcome Study., Hypertens. (Dallas, Tex. 1979). 47 (2006) 365–70. https://doi.org/10.1161/01.HYP.0000200699.74641.c5.

[6] M. Couade, M. Pernot, C. Prada, E. Messas, J. Emmerich, P. Bruneval, A. Criton, M. Fink, M. Tanter, Quantitative Assessment of Arterial Wall Biomechanical Properties Using Shear Wave Imaging, Ultrasound Med. Biol. 36 (2010) 1662–1676. https://doi.org/10.1016/j.ultrasmedbio.2010.07.004.

[7] T.M. Nguyen, M. Couade, J. Bercoff, M. Tanter, Assessment of viscous and elastic properties of sub-wavelength layered soft tissues using shear wave spectroscopy: Theoretical framework and in vitro experimental validation, IEEE Trans. Ultrason. Ferroelectr. Freq. Control. 58 (2011) 2305–2315. https://doi.org/10.1109/TUFFC.2011.2088.

[8] T. Roy, Guided Wave Inversion for Arterial Stiffness Estimation, North Carolina State University, 2021.

[9] W.T. Thomson, Transmission of elastic waves through a stratified solid medium, J. Appl. Phys. 21 (1950) 89–93. https://doi.org/10.1063/1.1699629.

[10] N.A. Haskell, The Dispersion of Surface Waves in Multilayered Anisotropic Media, 1953.

https://doi.org/10.1111/j.1365-246X.1970.tb01799.x.
[11] Knopoff L., A MATRIX METHOD FOR ELASTIC WAVE PROBLEMS, 1964.
[12] M.J. Randall, FAST PROGRAMS FOR LAYERED HALF-SPACE PROBLEMS, 1967.
[13] M.J. Lowe, Matrix Techniques for Modeling Ultrasonic Waves in Multilayered Media, IEEE Trans. Ultrason. Ferroelectr. Freq. Control. 42 (1995) 525–542. https://doi.org/10.1109/58.393096.
[14] M.J. Berliner, R. Solecki, Wave propagation in fluid-loaded, transversely isotropic cylinders. Part I. Analytical formulation, J. Acoust. Soc. Am. 99 (1996) 1841–1847. https://doi.org/10.1121/1.415365.
[15] H. Sato, H. Ogiso, Analytical method for guided waves propagating in a fluid-filled pipe with attenuation, Jpn. J. Appl. Phys. 52 (2013) 7. https://doi.org/10.7567/JJAP.52.07HC07.
[16] E. Kausel, Wave propagation in anisotropic layered media, Int. J. Numer. Methods Eng. 23 (1986) 1567–1578. https://doi.org/10.1002/nme.1620230811.
[17] S.K. Datta, R.L. Bratton, T. Chakraborty, A.H. Shah, Wave propagation in laminated composite plates, J. Acoust. Soc. Am. 83 (1988) 2020–2026. https://doi.org/10.1121/1.396382.
[18] L. Gavrić, Computation of propagative waves in free rail using a finite element technique, J. Sound Vib. 185 (1995) 531–543. https://doi.org/10.1006/jsvi.1995.0398.
[19] L. Gry, Dynamic modelling of railway track based on wave propagation, J. Sound Vib. 195 (1996) 477–505. https://doi.org/10.1006/jsvi.1996.0438.
[20] H. Taweel, S.B. Dong, M. Kazic, Wave reflection from the free end of a cylinder with an arbitrary cross-section, Int. J. Solids Struct. 37 (2000) 1701–1726. https://doi.org/10.1016/S0020-7683(98)00301-1.
[21] X. Han, G.R. Liu, Z.C. Xi, K.Y. Lam, Transient waves in a functionally graded cylinder, Int. J. Solids Struct. 38 (2001) 3021–3037. https://doi.org/10.1016/S0020-7683(00)00219-5.
[22] T. Hayashi, K. Kawashima, Z. Sun, J.L. Rose, Analysis of flexural mode focusing by a semianalytical finite element method, J. Acoust. Soc. Am. 113 (2003) 1241–1248. https://doi.org/10.1121/1.1543931.
[23] A. Jensen, N.B. Svendsen, Calculation of Pressure Fields from Arbitrarily Shaped, Apodized, and Excited Ultrasound Transducers, IEEE Trans. Ultrason. Ferroelectr. Freq. Control. 39 (1992).
[24] J.A. Jensen, Field: A Program for Simulating Ultrasound Systems, Med. Biol. Eng. Comput. 34 (1996) 351–353.
[25] I. Nenadic, M. Urban, J. Greenleaf, J.L. Gennisson, M. Bernal, M. Tanter, Ultrasound elastography for biomedical applications and medicine, Wiley, 2016. https://doi.org/10.1002/9781119021520.
[26] E. Kausel, R. Peek, DYNAMIC LOADS IN THE INTERIOR OF A LAYERED STRATUM: AN EXPLICIT SOLUTION, Bull. Seismol. Soc. Am. 72 (1982) 1459–1481.
[27] J.L. Tassoulas, E. Kausel, Elements for the numerical analysis of wave motion in layered strata, Int. J. Numer. Methods Eng. 19 (1983) 1005–1032. https://doi.org/10.1002/nme.1620190706.
[28] M.N. Guddati, K.-W. Lim, Continued fraction absorbing boundary conditions for convex polygonal domains, Int. J. Numer. Methods Eng. 66 (2006) 949–977. https://doi.org/10.1002/nme.1574.

[29] M. Guddati, K. Lim, M.A. Zahid, Perfectly matched discrete layers for unbounded domain modeling, in: F. Magoulès (Ed.), Comput. Methods Acoust. Probl., Saxe-Coburg Publications, Stirlingshire, UK, 2008: pp. 69–98. https://doi.org/http://dx.doi.org/10.4203/csets.18.3.

[30] M.W. Urban, A.V. Astaneh, W. Aquino, J.F. Greenleaf, M.N. Guddati, Measured wave dispersion in tubes excited with acoustic radiation force matches theoretical guided wave dispersion, IEEE Int. Ultrason. Symp. IUS. 2016-Novem (2016) 8–11. https://doi.org/10.1109/ULTSYM.2016.7728821.

[31] J.R. Doherty, G.E. Trahey, K.R. Nightingale, M.L. Palmeri, Acoustic radiation force elasticity imaging in diagnostic ultrasound, IEEE Trans. Ultrason. Ferroelectr. Freq. Control. 60 (2013) 685–701. https://doi.org/10.1109/TUFFC.2013.2617.

[32] S. Savadatti, M.N. Guddati, A finite element alternative to infinite elements, Comput. Methods Appl. Mech. Eng. 199 (2010) 2204–2223. https://doi.org/10.1016/j.cma.2010.03.018.

[33] A.V. Astaneh, M.W. Urban, W. Aquino, J.F. Greenleaf, M.N. Guddati, Arterial waveguide model for shear wave elastography: implementation and in vitro validation, Phys. Med. Biol. 62 (2017) 5473–5494. https://doi.org/10.1088/1361-6560/aa6ee3.

[34] T. Roy, M.W. Urban, Y. Xu, J.F. Greenleaf, M.N. Guddati, Multimodal guided wave inversion for arterial stiffness: methodology and validation in phantoms, Phys. Med. Biol. 66 (2021) 115020. https://doi.org/10.1088/1361-6560/ac01b7.

[35] T. Roy, M.N. Guddati, Shear wave dispersion analysis of incompressible waveguides, J. Acoust. Soc. Am. 149 (2021) 972–982. https://doi.org/10.1121/10.0003430.